Research article

Anhydrous proton-conducting imidazole triflate-SiO₂ composite

Tran Anh Tu [a,b], Nguyen Huu Huy Phuc [a,b,*]

[a] *Ho Chi Minh City University of Technology (HCMUT), 268 Ly Thuong Kiet Str., Dist. 10, Ho Chi Minh City, Vietnam*
[b] *Vietnam National University Ho Chi Minh City, Linh Trung Ward, Thu Duc Dist., Ho Chi Minh City, Vietnam*

ABSTRACT

ImidazoleTriflate (ITF)—SiO₂ composites xITF-(100-x)SiO₂ were prepared by planetary ball-milling method. The structure of the composites was studied by TG-DTA, XRD and FT-IR methods. The ionic conductivity was assessed by alternative current (AC) electrochemical impedance measurement. From XRD results, the crystal size of imidazole triflate became smaller as its loading in xITF-(100-x)SiO₂ decreased. With $x = 40$ weight percent, the calculated crystal size was about 7.3 nm. FT-IR spectra showed the existence of $CF_3SO_3\cdots H^+$ ion aggregates and imidazole—proton bonds. The electrical conductivity of sample $x = 50$ was about 6.3×10^{-3} Scm⁻¹ at 130 °C under anhydrous condition and about 30 times higher than that of sample $x = 100$.

1. Introduction

The development of materials with high protic conductivity under anhydrous condition is essential for the development of fuel cells operating at intermediate temperatures. Among the earliest developed substances, the mechanically synthesized $KHSO_4$–$H_3PW_{12}O_{40}$ (KHS–WPA) composites exhibited relatively high dried-proton conductivity [1]. The 95KHS·5WPA (mol%) composite showed very high conductivity of 1.3×10^{-2} to 2.4×10^{-3} S cm⁻¹ in the temperature range of 160 °C to 80 °C under dry N₂ atmosphere. New chemical interaction via ion-exchange and hydrogen bonding between HSO_4^- and partially K-substituted WPA were the main causes of the improved conductivity in composites. The same group then found that the proton conductivity of the $MHSO_4$–$H_4SiW_{12}O_{40}$ (M = K, NH₄, Cs) composites were about 3-digit of magnitude higher than that of the starting materials, $MHSO_4$ and $H_4SiW_{12}O_{40}$ [2]. Besides the heteropoly acid, $CsH_5(PO_4)_2$ is the most efficient inorganic electrolyte among solid proton conductors, but its usage is suffered from a low melting temperature, about 150 °C. The formation of P–OH⋯F hydrogen bonds the in $CsH_5(PO_4)_2$–LaF_3 composite inhibited the rotation of the phosphate anions in $CsH_5(PO_4)_2$, and thermomechanical stability of $CsH_5(PO_4)_2$ was subsequently improved [3]. The proton conductivity of $CsH_5(PO_4)_2$–LaF_3 composite reached the value of about 3.0×10^{-2} S cm⁻¹ at 150 °C under anhydrous condition.

In addition to inorganic composites, inorganic crystals also exhibited good protonic conductivity in non-humidified environment. The layered zirconium phosphate, $(NH_4)_2[ZrF_2(HPO_4)_2]$ (ZrP-1), contained an extremely dense network of two-dimensional hydrogen-bond [4]. ZrP-1 exhibited proton conduction behaviors at two different temperature regions. The anhydrous conductivity reached 1.1×10^{-5} S cm⁻¹ at 230 °C. Ammonium borosulfate, $NH_4[B(SO_4)_2]$, also showed high proton conductivity under non-humidified condition [5]. This solid acid was a coordination polymer and consisted of 1D hydrogen-bonded $NH_4^+ \cdots{}^1_\infty[B(SO_4)_{4/2}]^-$ chains. The proton conductivity of the polycrystalline monolithic disc was about 10^{-4} Scm⁻¹ at 25 °C and 10^{-2} Scm⁻¹ at 180 °C in ambient air humidity (about 45% at 25 °C). The proton conductivity of single crystal $(NH_4)_3H(SO_4)_2$ exhibited the anisotropy of the monoclinic phase at low temperature and rhombohedral phase at high temperature [6]. The superionic conductivity, about 10^{-2} S cm⁻¹ at 140 °C, was found in the hexagonal (001) plane.

Organic–inorganic composites also showed high proton conductivity in anhydrous conditions. Imidazole heterocyclic (ImH, $C_3H_4N_2$) and its relative compounds are known for their high protonic conductivity under anhydrous condition. ImH had high conductivity of about 10^{-3} Scm⁻¹ in the liquid state (above 90 °C) [7]. However, the conductivity of solid ImH dropped to about 10^{-8} Scm⁻¹. Therefore, many attempts have been made to overcome the temperature-dependence disadvantages, i.e. forming composites with acids. Formation of an acid-base composite material between ImiH and various organic acids is the most common route due to the large number of organic acids and the simple synthesis process. Methanesulfonic acid, dicarboxylic acids (succinic acid, glutaric acid), phthalic acid were used to form proton conduction salts with imidazole [8, 9, 10, 11, 12, 13]. ImH in ImiH—$Al(H_2PO_4)_3$ composite remained solid up to 130 °C without any sudden drop in conductivity in the region below 90 °C [14]. The salt formation ($ImH_2^+ \cdot H_2PO_4^-$) in ImiH—$Al(H_2PO_4)_3$ was the

cause of the enhanced low-temperature proton conductivity and thermal stability of ImH in the composite. Loading ImiH into the pore system of biphenylene-bridged Periodic-Mesoporous-Organosilica (PMO) and its sulfonated derivatives (s-PMO) improved the ionic conductivity of the host materials and thermal stability of ImiH; its evaporation only started at 138 and 158 °C in ImiH@PMO and ImiH@s-PMO, respectively [15].

Silica is a common filler used in fuel cells, mainly for proton exchange membrane fuel cells, and it has an important role in enhancing fuel cell performance by improving the membrane properties. The incorporation of silica into the membrane matrix improved the thermal stability, mechanical strength, water retention and proton conductivity [16, 17, 18]. In addition, proton exchange membranes have poor hygroscopicity under low humidity conditions, and this causes a severe decline in hydration dependence proton conductivity [19]. One of the solutions to this problem is addition of bifunctional (ceramic/hygroscopic) filler into the membrane. Silica modifier enhanced the proton conductivity of Nafion in low humidity condition (20–60% RH, 110–120 °C) [20]. Phosphotungstic acid supported on silica also improved the proton conductivity of Nafion at low humidity (20–60% RH) and 110 °C [21].

These successful results prompted us to search for novel composites that contains ImiH and exhibits high proton conductivity under anhydrous conditions. In this study, we report the preparation and characterization of Imidazole Triflate (ITF)-SiO_2 composite. The composites were prepared by planetary ball-milling method and characterized by TG-DTA, XRD and FT-IR methods. The electrical conductivity of the pelletized composites was calculated from the AC impedance spectroscopy results, and the conductivity of 50ITS-50SiO_2 (weight percent) was about thirty times higher than that of the ITS sample.

2. Experimental

Dehydrated Heptane, Silica fumed (SiO_2) and Imidazole Triflate (97%) were purchased from Sigma Aldrich. SiO_2 and Imidazole Triflate were dried at 110 °C for 24 h, stored in Ar-filled glove-box for one week before the experiments.

Composite samples were prepared by planetary ball-milling method. A total of 2 g of ITF and SiO_2 to form xITF-(100-x)SiO_2 (weight percent) were weighed and placed in a zirconia pot (45 ml) with 45 g of zirconia balls (4 mm), and 5 ml of heptane. The pots were rotated at 450 rpm for 6 h using a Pulverisette 7 (Fritsch). The resulting slurries was recovered, dried under reduced pressure at room temperature and 120 °C. The received powder samples were stored in Ar-filled glove boxes for other experiments.

The structure of the prepared samples was characterized by thermogravimetry - differential thermal analysis (TG−DTA; EVO II, Rigaku), X-ray diffraction (XRD; ULTIMA IV, Rigaku), Fourier transform infrared spectroscopy (FT-IR; FT/IR-6100, JASCO).

The temperature dependence of the sample's ionic conductivity was investigated using alternating-current impedance spectroscopy (VSP, Biologic) from 1 MHz to 10 Hz under dry N_2 flow. Samples used to measure ionic conductivity was prepared by uniaxially cold pressing approximately 250 mg of powder into pellet (diameter of 10.0 mm) at 110 MPa and sandwiching between stainless-steel (SUS) electrodes. The temperature was gradually increased, from room temperature to 130 °C, while each temperature was held for 1 h prior to measurement.

3. Results and discussion

Figure 1 showed the TG-DTA curves of ball-milled ITF and 60ITF-40SiO_2 composite. The results demonstrated the high thermal stability of these samples. Ball-milled ITF and 60ITF-40SiO_2 composite showed decomposition initiation at 338 and 333 °C, respectively. The DTA curve of ball-milled ITF had four endothermic peaks located at 34 (I), 104 (II), 161 (III), and 192 °C (IV). There was no remarkable weight loss associated with peak (IV), so it represented the melting point of ITF. Peaks (I, II, III) could be assigned to the phase transition of ITF.
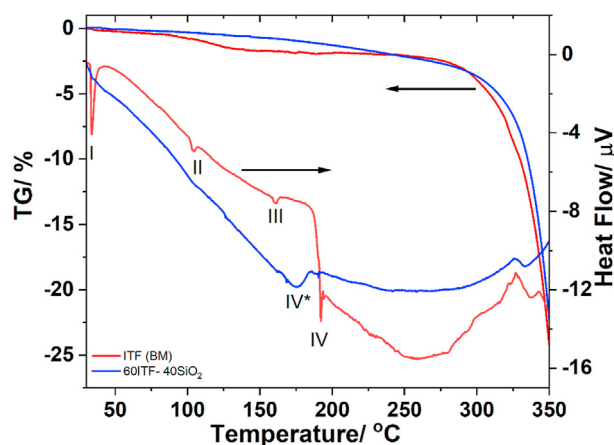

Figure 1. TG-DTA curves of the ball-milled ITF and the prepared 60ITF-40SiO_2.

The phase transition was also observed in other organic ionic plastic crystals (OIPC), i.e. 2-methylimidazolium triflate, 2-methylimidazolinium triflate, imidazolium triflate, and N,N-dimethyl pyrrolidinium tetrafluoroborate [13, 22, 23]. The melting point of ITS in 60ITF-40-SiO_2 composite was 176 °C (IV*), which was slightly lower than that of the ball-milled ITF. However, the phase transition almost disappeared in the DTA curve of the 60ITF-40SiO_2 composite. Therefore, the composite formation with SiO_2 suppressed the phase transition of ITF.

Figure 2 showed the XRD patterns of the intrinsic ITF, ball-milled ITF and the prepared xITF-(100-x)SiO_2. The inset showed the crystalline size of ITF in the prepared samples, which were calculated using Scherrer equation. The structure of ITF belonged to the orthorhombic space group, Pbca, with cell parameters $a = 7.959$ Å, $b = 11.038$ Å, and $c = 16.159$ Å [24]. Imidazole methanesulfonate also crystallized in the orthorhombic space group, Pbca, with cell parameters $a = 7.918$ Å, $b = 11.040$ Å, and $c = 16.086$ Å [25]. Therefore, the structure of ITF was resembled to that of imidazole methanesulfonate. The XRD pattern of intrinsic ITF obtained in our study was similar to that of imidazole methanesulfonate measured at 25 °C [8, 26]. The XRD pattern of ball-milled ITF had all the features of intrinsic ITF with slight shift in the values of 2θ due to temperature-induced lattice expansion. Temperature dependence of crystal symmetry was reported for several OIPCs, such as tetraethyl phosphonium fluorohydrogenate salt, tetrabutylammonium
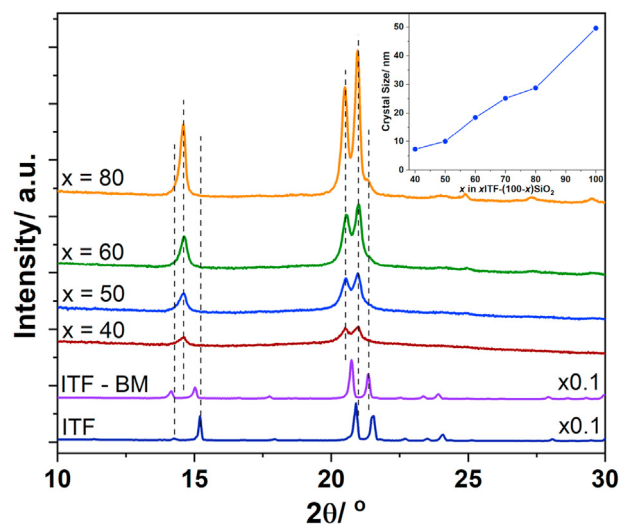

Figure 2. XRD patterns of the intrinsic ITF, ball-milled ITF and the prepared xITF-(100-x)SiO_2. The small inset showed ITF's crystal size of the prepared samples.
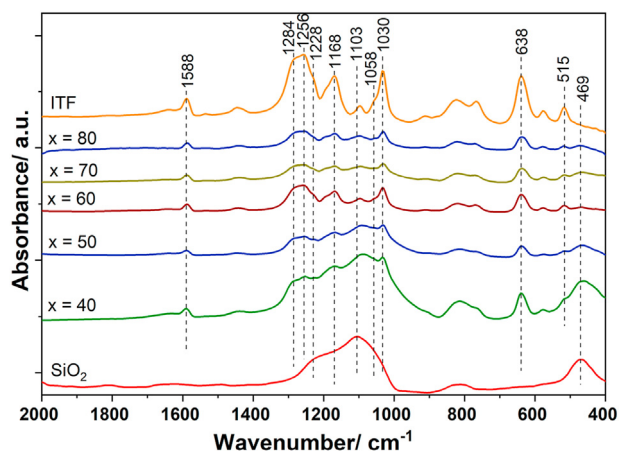
Figure 3. FT-IR spectra of the intrinsic ITF, SiO$_2$ and the prepared xITF-(100-x)SiO$_2$.

iodide [27, 28]. Peaks of orthorhombic ITF at positions 2θ = 14.1 and 15.0° were no longer observed in XRD patterns of xITF-(100-x)SiO$_2$ composites. In addition, a new peak at position 2θ = 14.6° appeared in all the diffraction patterns of the composites. Those observation indicated that there was an increase in space group symmetry of ITF in composites compared to that of intrinsic and ball-milled ITF. The XRD and TG-DTA results (Figure 1), illustrated that the high temperature phase of ITF was stabilized to room temperature in xITF-(100-x)SiO$_2$. The peak at 2θ = 21.1° in the diffraction patterns of x = 60 and 80 was similar to the peak of the ball-milled ITF. The fitting result (Figure S1) revealed the existence of a peak at 2θ = 20.7° in the diffraction pattern of x = 80. Thus, the peaks at 2θ = 20.7 and 21.1° indicated the presence of unsupported ball-milled ITF in samples $x \geq 60$. In addition, results from the Scherrer equation showed the dependence of ITF crystal size on its fraction in xITF-(100-x)SiO$_2$ composites, implying that ITF and SiO$_2$ did not exist separately in the composite, but ITF was attached to the surface of SiO$_2$ particles.

Figure 3 illustrated the IR spectra of SiO$_2$, ball-milled ITF and xITF-(100-x)SiO$_2$ composites. SiO$_2$ showed absorption bands at 469 and 1103
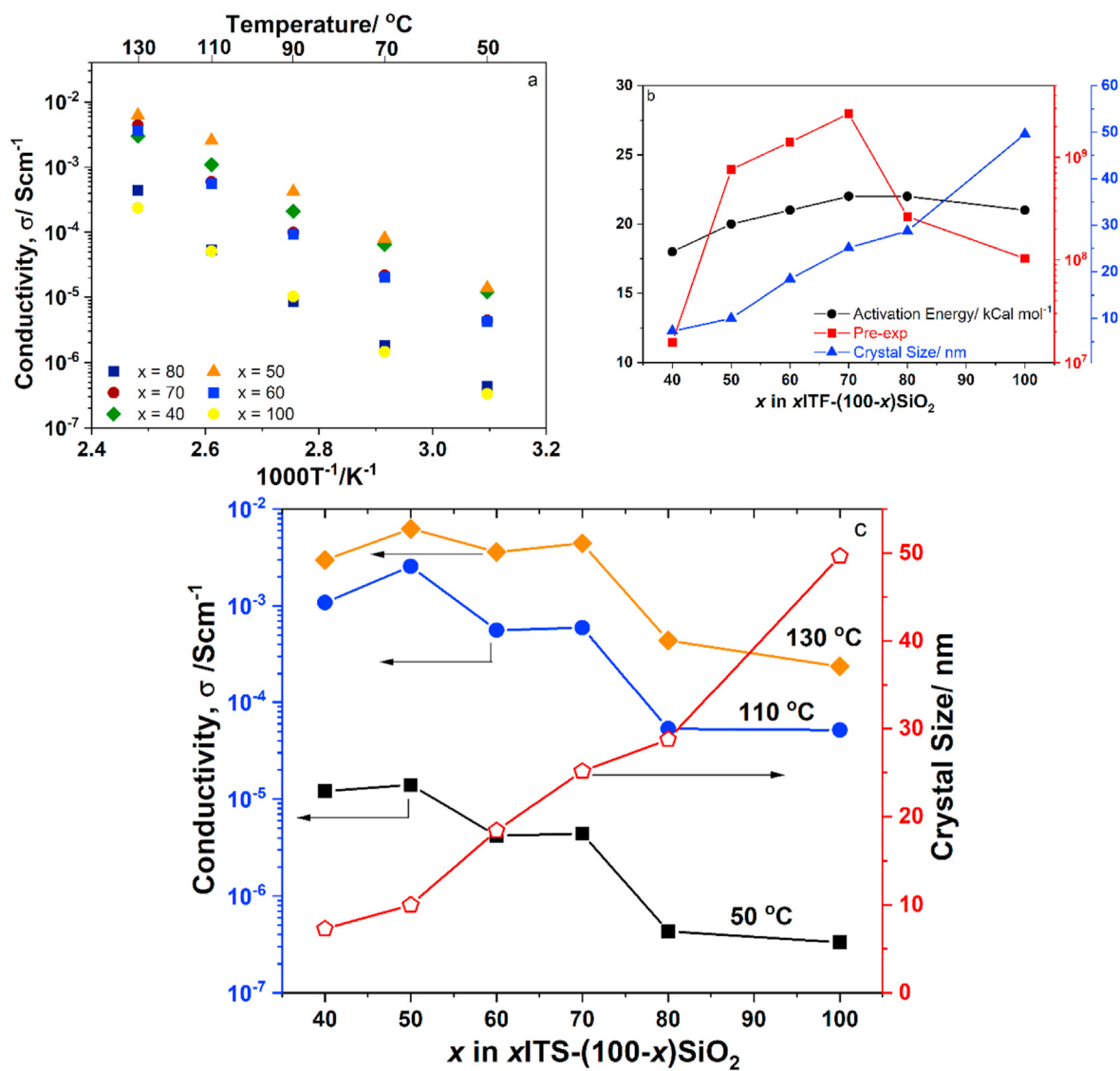

Figure 4. Conduction properties of the prepared xITF-(100-x)SiO$_2$. a) Temperature dependence ionic conductivity; b) Activation energy (closed circle), ITF's crystal size (closed triangle), and pre-exponential factor A (closed square) as a function of x; c) Ionic conductivity at different temperatures and ITF's crystal size as a function of x.

cm^{-1} that were attributed to the vibration of O–Si–O [29]. These bands became smaller in 40ITF-60SiO$_2$, 50ITF-50SiO$_2$ and disappeared in samples $x \geq 60$, indicating the formation of core-shell structure. The absorption bands at 638, 1168, and 1284 cm^{-1} could be assigned to asymmetric bending, stretching, and symmetric stretching of SO$_3^-$ of ITF [30, 31, 32]. The bands observed at 1058 and 1228 cm^{-1} were attributed to symmetric stretching of CF$_3$ [30, 31, 33]. The bands at 515, 1030, and 1256 cm^{-1} corresponded to the CF$_3$SO$_3^-$···H$^+$ ion aggregates [32, 33]. The band at 1588 cm^{-1} was attributable to stretching of protonated imidazole ring [34]. Thus, the FT-IR results illustrated the presence of two types of ion aggregates, CF$_3$SO$_3^-$···H$^+$ and ImiH···H$^+$, in the prepared samples.

Figure 4a showed the temperature dependence of the ionic conductivity of xITF-(100-x)SiO$_2$ composites. The resistivity of ball-milled ITF (x = 100) at room temperature was too large and became small enough to be measured at 50 °C. Sample $x = 80$ had a similar conductivity to $x = 100$. Samples $40 \leq x \leq 70$ had their resistivity small enough to be measured at room temperature. The proton conductivity of the $40 \leq x \leq 70$ samples was about 20–30 times higher than that of $x = 100$ and 80 in the temperature range of 50–130 °C. The temperature dependence of the ionic conductivity of all samples followed the Arrhenius equation; therefore, the activation energy and pre-exponential factor were calculated and plotted in Figure 4b. The activation energy E$_a$ of all samples ranged from 18 to 22 kCal mol^{-1}. The high values of E$_a$ illustrated the strong temperature dependent of the conductivity of all samples. Figure 4b showed the correlation between ITF crystal size in samples $40 \leq x \leq 70$ and activation energy, pre-exponential values. Better proton conductivity of samples $40 \leq x \leq 70$ could be attributed to high proton mobility, which were the result of composite formation. Samples $x = 80$ and 100 contained un-supported ITS, as shown in Figure 2, and had similar conductivity, activation energy, and pre-exponential values. Figure 4c showed the dependence of proton conductivity and ITS crystal size on the composite composition. The proton conductivity of sample $x = 80$ was nearly the same as that of sample $x = 100$ although the ITF crystal sizes in the two samples were 28.76 and 49.63 nm, respectively. Besides, the XRD analysis results indicated the existence of free ITF in sample $x = 80$. Thus, the low ionic conductivity of the free ITF was the cause that made the ionic conductivity of sample $x = 80$ close to that of sample $x = 100$. In general, the activation energy and pre-exponential value were proportional to the change in ITF crystal size in the range of $40 \leq x \leq 70$; but the change of ionic conductivity was inversely proportional to the change of ITF crystal size when $40 \leq x \leq 80$. Thus, proton movement at the crystalline interface might be the main cause of the increase conductivity.

4. Conclusion

In summary, xITF-(100-x)SiO$_2$ composites were successfully fabricated by planetary ball-milling method. The TG-DTA and XRD results revealed the presence of a high temperature phase of ITF in the composites at room temperature. CF$_3$SO$_3^-$···H$^+$ and ImiH···H$^+$ were the proton-containing bonds in the samples. The proton conductivity of $40 \leq x \leq 70$ was about 20–30 times higher than those of $x = 80$ and 100. The change of ionic conductivity was inversely proportional to the change of ITF crystal size when $40 \leq x \leq 80$, which implied that proton movement at the crystalline interface might be the main cause of the increase conductivity.

Declarations

Author contribution statement

Tran Anh Tu: Performed the experiments; Contributed reagents, materials, analysis tools or data.

Nguyen Huu Huy Phuc: Conceived and designed the experiments; Analyzed and interpreted the data; Wrote the paper.

Data availability statement

Data will be made available on request.

Declaration of interests statement

The authors declare no conflict of interest.

Additional information

Supplementary content related to this article has been published online at https://doi.org/10.1016/j.heliyon.2022.e12527.

References

[1] A. Matsuda, S.-y. Oh, V.H. Nguyen, Y. Daiko, G. Kawamura, H. Muto, Anhydrous proton conductivity of KHSO$_4$–H$_3$PW$_{12}$O$_{40}$ composites and the correlation with hydrogen bonding distance under ambient pressure, Electrochim. Acta 56 (2011) 9364–9369.

[2] S.-y. Oh, K. Kawai, G. Kawamura, H. Muto, A. Matsuda, Characterization of mechanochemically synthesized MHSO$_4$–H$_4$SiW$_{12}$O$_{40}$ composites (M=K, NH$_4$, Cs), Mater. Res. Bull. 47 (2012) 2931–2935.

[3] J. Xiong, Y. Huang, J. Li, L. Ma, G. Xu, Z. Liu, W. Cai, H. Cheng, A novel thermomechanically stable LaF$_3$CsH$_5$(PO$_4$)$_2$ composite electrolyte with high proton conductivity at elevated temperatures over 150 °C, J. Energy Chem. 30 (2019) 114–120.

[4] D. Gui, T. Zheng, J. Xie, Y. Cai, Y. Wang, L. Chen, J. Diwu, Z. Chai, S. Wang, Significantly dense two-dimensional hydrogen-bond network in a layered zirconium phosphate leading to high proton conductivities in both water-assisted low-temperature and anhydrous intermediate-temperature regions, Inorg. Chem. 55 (2016) 12508–12511.

[5] M.D. Ward, B.L. Chaloux, M.D. Johannes, A. Epshteyn, Facile proton transport in ammonium borosulfate-an unhumidified solid acid polyelectrolyte for intermediate temperatures, Adv. Mater. 32 (2020), e2003667.

[6] Y.J. Sohn, K.M. Sparta, M. Meven, G. Roth, G. Heger, Superprotonic conductivity of (NH$_4$)$_3$H(SO$_4$)$_2$ in the high-temperature phase, Solid State Ionics 252 (2013) 116–120.

[7] A. Kawada, A.R. McGhie, M.M. Labes, Protonic conductivity in imidazole single crystal, J. Chem. Phys. 52 (1970) 3121–3125.

[8] J. Luo, O. Conrad, I.F.J. Vankelecom, Imidazolium methanesulfonate as a high temperature proton conductor, J. Mater. Chem. 1 (2013) 2238–2247.

[9] Y. Sunairi, A. Ueda, J. Yoshida, K. Suzuki, H. Mori, Anisotropic proton conductivity arising from hydrogen-bond patterns in anhydrous organic single crystals, imidazolium carboxylates, J. Phys. Chem. C 122 (2018) 11623–11632.

[10] S. Dekura, Y. Sunairi, K. Okamoto, F. Takeiri, G. Kobayashi, Y. Hori, Y. Shigeta, H. Mori, Effects of mechanical grinding on the phase behavior and anhydrous proton conductivity of imidazolium hydrogen succinate, Solid State Ionics 372 (2021), 115775.

[11] Y. Hori, S. Dekura, Y. Sunairi, T. Ida, M. Mizuno, H. Mori, Y. Shigeta, Proton conduction mechanism for anhydrous imidazolium hydrogen succinate based on local structures and molecular dynamics, J. Phys. Chem. Lett. 12 (2021) 5390–5394.

[12] S. Zięba, A. Dubis, P. Ławniczak, A. Gzella, K. Pogorzelec-Glaser, A. Łapiński, Effect of counter ions on physical properties of imidazole-based proton conductors, Electrochim. Acta 306 (2019) 575–589.

[13] H. Zhu, M. Forsyth, Ion vacancies and transport in 1-methylimidazolium triflate organic ionic plastic crystal, J. Phys. Chem. Lett. 11 (2020) 510–515.

[14] M. Nakayama, Y. Sugiura, T. Hayakawa, M. Nogami, A novel proton conductor of imidazole-aluminium phosphate hybrids in the solid state. Phys. Chem. Chem. Phys. : Phys. Chem. Chem. Phys. 13 (2011) 9439–9444.

[15] L. Wu, Y. Yang, Y. Ye, Z. Yu, Z. Song, S. Chen, L. Chen, Z. Zhang, S. Xiang, Loading acid–base pairs into periodic mesoporous organosilica for high anhydrous proton conductivity over a wide operating temperature window. ACS Appl. Energy Mater. 1 (2018) 5068–5074.

[16] P. Martina, R. Gayathri, M.R. Pugalenthi, G. Cao, C. Liu, M.R. Prabhu, Nanosulfonated silica incorporated SPEEK/SPVdF-HFP polymer blend membrane for PEM fuel cell application, Ionics 26 (2020) 3447–3458.

[17] K.H. Lee, J.Y. Chu, A.R. Kim, D.J. Yoo, Effect of functionalized SiO_2 toward proton conductivity of composite membranes for PEMFC application, Int. J. Energy Res. 43 (2019) 5333–5345.

[18] M. Ranjani, M. Pannipara, A.G. Al-Sehemi, A. Vignesh, G.G. kumar, Chitosan/ sulfonated graphene oxide/silica nanocomposite membranes for direct methanol fuel cells, Solid State Ionics 338 (2019) 153–160.

[19] A.R. Kim, M. Vinothkannan, D.J. Yoo, Artificially designed, low humidifying organic–inorganic (SFBC-50/FSiO_2) composite membrane for electrolyte applications of fuel cells, Composites Part B: Engineering 130 (2017) 103–118.

[20] S.L. Guoxiao Xu, Li Jing, Liu Zhao, Ying Li, Jie Xiong, Weiwei Cai, Konggang Qu, Hansong Cheng, Targeted filling of silica in Nafion by a modified in situ sol–gel method for enhanced fuel cell performance at elevated temperatures and low humidity, Chem. Commun. 55 (2019) 5499–5502.

[21] G. Xu, S. Xue, Z. Wei, J. Li, K. Qu, Y. Li, W. Cai, Stabilizing phosphotungstic acid in Nafion membrane via targeted silica fixation for high-temperature fuel cell application, Int. J. Hyd. Energy 46 (2021) 4301–4308.

[22] A.L. Chong, H. Zhu, K.M. Nairn, M. Forsyth, D.R. MacFarlane, Enhancing Solid-state conductivity through acid or base doping of protic imidazolium and imidazolinium triflate salts, J. Phy. Chem. C 121 (2017) 27849–27859.

[23] J.M. Pringle, J. Adebahr, D.R. MacFarlane, M. Forsyth, Unusual phase behaviour of the organic ionic plastic crystal N,N-dimethylpyrrolidinium tetrafluoroborate, Phys. Chem. Chemical Phy. : PCCP 12 (2010) 7234–7240.

[24] N.E. De Almeida, G.R. Goward, Proton dynamics in sulfonated ionic salt composites: Alternative membrane materials for proton exchange membrane fuel cells, J. Power Sources 268 (2014) 853–860.

[25] G.R. Goward, K. Saalwächter, I. Fischbach, H.W. Spiess, Reorientation phenomena in imidazolium methyl sulfonate as probed by advanced solid-state NMR, Solid State Nucl. Magn. Reson. 24 (2003) 150–162.

[26] J. Luo, T.V. Tan, O. Conrad, I.F. Vankelecom, 1H-1,2,4-Triazole as solvent for imidazolium methanesulfonate, Phys. Chem. Chem. Phys : PCCP 14 (2012) 11441–11447.

[27] T. Enomoto, S. Kanematsu, K. Tsunashima, K. Matsumoto, R. Hagiwara, Physicochemical properties and plastic crystal structures of phosphonium fluorohydrogenate salts, Phy. Chem. Chemical Physics : PCCP 13 (2011) 12536–12544.

[28] R. Asayama, J. Kawamura, T. Hattori, Phase transition and ionic transport mechanism of ($C_4H_9)_4NI$, Chem. Phy. Letters 414 (2005) 87–91.

[29] S. Ishak, S. Mandal, H.-S. Lee, J.K. Singh, Effect of core-shell ratio on the thermal energy storage capacity of SiO2 encapsulated lauric acid, J. Energy Storage 42 (2021), 103029.

[30] R. Kumar, S.S. Sekhon, Conductivity, FTIR studies, and thermal behavior of PMMA-based proton conducting polymer gel electrolytes containing triflic acid, Ionics 19 (2013) 1627–1635.

[31] S. Sharma, D. Pathak, N. Dhiman, R. Kumar, M. Kumar, FTIR, thermal and ionic conductivity studies of nanocomposite polymer electrolytes, Surf. Innov. 7 (2019) 51–58.

[32] A. Aslan, S.Ü. Çelik, Ü. Şen, R. Haser, A. Bozkurt, Intrinsically proton-conducting poly(1-vinyl-1,2,4-triazole)/triflic acid blends, Electrochimica Acta 54 (2009) 2957–2961.

[33] R. Kumar, S. Sharma, D. Pathak, N. Dhiman, N. Arora, Ionic conductivity, FTIR and thermal studies of nano-composite plasticized proton conducting polymer electrolytes, Solid State Ionics 305 (2017) 57–62.

[34] B.B.D.H. Bonsor, R.L. Dean, J.L. Wood, Complex hydrogen bonded cations. The imdazole/imidazolium complex cation, Can. J. Chem. 54 (1976) 2458–2464.